ACS APPLIED MATERIALS & INTERFACES

Research Article

Cite This: ACS Appl. Mater. Interfaces 2018, 10, 18845−18856

www.acsami.org

Red Mn^{4+}-Doped Fluoride Phosphors: Why Purity Matters

Reinert Verstraete,[†,‡] Heleen F. Sijbom,[†,‡] Jonas J. Joos,[†,‡] Katleen Korthout,[†,‡] Dirk Poelman,[†,‡] Christophe Detavernier,[‡,§] and Philippe F. Smet*[,†,‡]

[†]LumiLab, Department of Solid State Sciences, [‡]Center for Nano- and Biophotonics (NB-Photonics), and [§]Conformal Coating of Nanomaterials (CoCooN), Department of Solid State Sciences, Ghent University, 9000 Ghent, Belgium

Supporting Information

ABSTRACT: Traditional light sources, e.g., incandescent and fluorescent lamps, are currently being replaced by white light-emitting diodes (wLEDs) because of their improved efficiency, prolonged lifetime, and environmental friendliness. Much effort has recently been spent to the development of Mn^{4+}-doped fluoride phosphors that can enhance the color gamut in displays and improve the color rendering index, luminous efficacy of the radiation, and correlated color temperature of wLEDs used for lighting. Purity, stability, and degradation of fluoride phosphors are, however, rarely discussed. Nevertheless, the typical wet chemical synthesis routes (involving hydrogen fluoride (HF)) and the large variety of possible Mn valence states often lead to impurities that drastically influence the performance and stability of these phosphors. In this article, the origins and consequences of impurities formed during synthesis and aging of K_2SiF_6:Mn^{4+} are revealed. Both crystalline impurities such as KHF_2 and ionic impurities such as Mn^{3+} are found to affect the phosphor performance. While Mn^{3+} mainly influences the optical absorption behavior, KHF_2 can affect both the optical performance and chemical stability of the phosphor. Moisture leads to decomposition of KHF_2, forming HF and amorphous hydrated potassium fluoride. As a consequence of hydrate formation, significant amounts of water can be absorbed in impure phosphor powders containing KHF_2, facilitating the hydrolysis of $[MnF_6]^{2-}$ complexes and affecting the optical absorption of the phosphors. Strategies are discussed to identify impurities and to achieve pure and stable phosphors with internal quantum efficiencies of more than 90%.

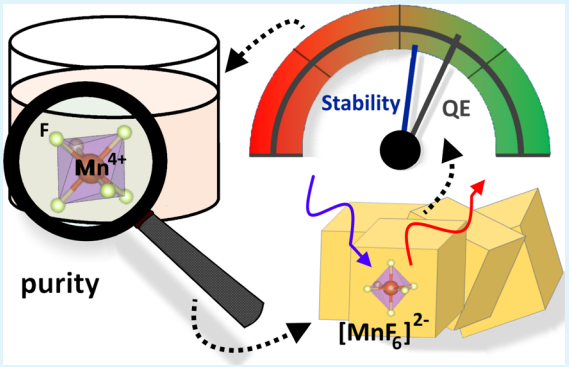

KEYWORDS: *fluoride phosphors, stability, purity, transition-metal dopants, LEDs*

INTRODUCTION

A new era in lighting and display applications has emerged with the development of white light-emitting diodes (wLEDs), which outperform the more traditional light sources such as incandescent or fluorescent lamps because of their high efficiency, prolonged lifetime, and environmental friendliness. Single-phosphor wLEDs consist of a blue-emitting InGaN light-emitting diode (LED) chip and a yellow-emitting photoluminescent material or phosphor, which converts a part of the blue light into light with a longer wavelength.[1,2] The combined emission of the LED chip and phosphor then yields white light. $Y_3Al_5O_{12}$:Ce^{3+} (YAG:Ce) is often used in single-phosphor wLEDs because of its high stability, quantum efficiency (QE), and very broad yellow emission spectrum.[3,4] Nevertheless, the obtained white light of YAG:Ce-based single-phosphor wLEDs is typically perceived as cold white light (correlated color temperature (CCT) > 6000 K) and the color rendering index (CRI) is too low (CRI < 80) for use in most lighting applications.[5,6] A lack of red emission lies at the origin of these high CCT and low CRI values, which can be compensated by adding a red phosphor. Although several red phosphors have been developed, only a small number meet the requirements for lighting and displays.[6] First, the emission of red phosphor materials should be minimal above 650 nm, as the human eye sensitivity above this wavelength is very low.[2] Second, the emission should preferably be saturated red, corresponding to a narrow emission band. Especially for use in display applications, saturated red phosphors are desirable as they enlarge the color gamut.[7,8] Apart from optical requirements, the stability of phosphors is a major concern. Degradation of phosphor materials due to heat, moisture, or light exposure causes a decreased light output and a color shift of the wLED with time.[9] To some extent, these effects can be counteracted by the encapsulation of the phosphor particles.[10−12] Considering the long expected lifetime of LEDs (>50 000 h), stability performance of phosphors becomes increasingly important.[13,14]

Several types of red phosphor have been evaluated for use in commercial wLEDs. Sulfide phosphors, e.g., (Sr,Ca)S:Eu^{2+},[15] show hydrolysis and release of H_2S when the material is subjected to heat and humidity.[16] Instead, more chemically

Received: January 23, 2018
Accepted: May 11, 2018
Published: May 11, 2018

DOI: 10.1021/acsami.8b01269
ACS Appl. Mater. Interfaces 2018, 10, 18845−18856

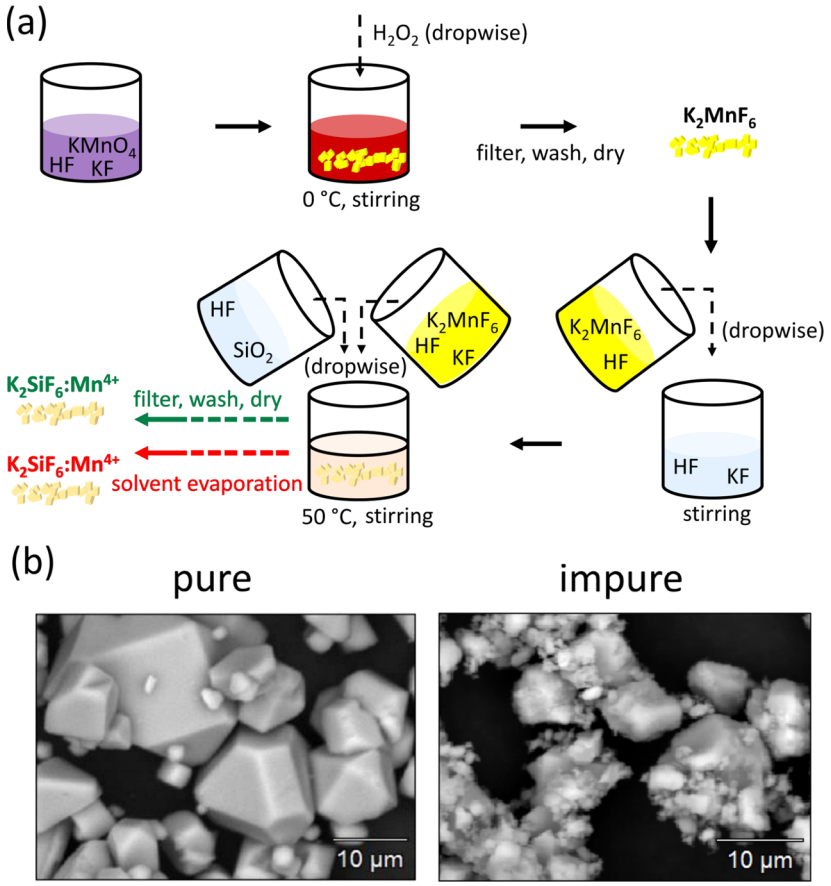

Figure 1. (a) Schematic representation of the two-step co-precipitation synthesis of K_2SiF_6:Mn^{4+}. (b) SEM images of pure and impure K_2SiF_6:Mn^{4+}.

stable nitride phosphors like $CaAlSiN_3$:Eu^{2+} [17] and $(Sr,Ba)_2Si_5N_8$:Eu^{2+} [18] have been used as the red component in wLEDs. However, with a few exceptions such as $Sr[LiAl_3N_4]$:Eu^{2+},[19] nitride phosphors have a broad red emission band, which extends considerably beyond 650 nm, lowering the attainable luminous efficacy of the radiation. In addition, Eu^{2+}-based phosphors are characterized by a small Stokes shift and broad excitation bands, which leads to reabsorption issues when used in a blend with yellow or green phosphors.[20] Therefore, a new class of rare-earth-free red fluoride phosphors has recently gained interest. Mn^{4+} is doped on the M-site of a fluoride host, forming compounds such as A_2MF_6:Mn^{4+} (A = K, Na, Sc, NH_4, Cs and M = Si, Ge, Ti, Sn, Zr, Hf), $KNaMF_6$:Mn^{4+}, $BaMF_6$:Mn^{4+} (M = Si, Ti, Ge, Sn), or $ZnMF_6 \cdot H_2O$ (M = Si, Ge).[21−34] The Mn^{4+} activator and its fluorine ligands form a $[MnF_6]^{2-}$ coordination complex that can be excited efficiently at around 450 nm with minimal absorption above 500 nm. From this, saturated red emission below 650 nm is obtained. Hence, fluoride phosphors are promising candidates for use in wLEDs, provided that a good chemical stability can be ensured. Amongst the fluoride phosphors, K_2SiF_6:Mn^{4+} is a frequently studied material.[35] K_2SiF_6:Mn^{4+} has a good thermal quenching behavior compared with more conventional red nitride phosphors, although saturation effects arise at high excitation fluxes due to the long luminescence decay time of the parity- and spin-forbidden d−d transition.[36] Nevertheless, this phosphor is a promising candidate to be used in display backlighting or in remote wLEDs where a phosphor plate is spatially separated from the LED chip, lowering the excitation flux. Despite its promising applications, synthesis of K_2SiF_6:Mn^{4+} proves to be challenging. Fluoride phosphors are commonly produced by wet chemical methods involving hydrogen fluoride (HF). A drawback of these methods is the vulnerability to form impurities affecting phosphor properties, such as thermal quenching, concentration quenching,[37] optical absorption, quantum efficiency, and chemical stability. Hence, the primary challenge exists in synthesizing impurity-free K_2SiF_6:Mn^{4+}. Because of the large range of possible Mn valence states, reaching from 7+ to 0, secondary Mn valences can occur that influence the optical behavior of the phosphor. Secondary Mn valence states often remain unnoticed, as they do not necessarily influence the X-ray diffraction (XRD) pattern. On the other hand, crystalline and amorphous impurity phases can also occur, which can lower both the optical and stability performance of the phosphor. In this article, the origin and consequences of common impurities in K_2SiF_6:Mn^{4+}, both before and after aging, are investigated.

EXPERIMENTAL SECTION

Common synthesis methods of K_2SiF_6:Mn^{4+} include chemical etching, cocrystallization, and (co)precipitation.[35] Here, a two-step co-precipitation method is used, which allows an enhanced control of the Mn valence state. A schematic representation of the synthesis steps is shown in Figure 1a. The first step of this method includes the synthesis of K_2MnF_6 as a precursor by the method of Bode and Bandte.[38] Subsequently, this inhouse synthesized K_2MnF_6 is dissolved in 40% HF (Sigma-Aldrich), after which this solution is dropwise added to a solution of potassium fluoride (KF, 99%, Alfa Aesar) in 40% HF. A third 40% HF solution is used to dissolve SiO_2 (99.5%, Alfa Aesar). In the next step, both KF/K_2MnF_6 and SiO_2 solutions are

DOI: 10.1021/acsami.8b01269
ACS Appl. Mater. Interfaces 2018, 10, 18845−18856

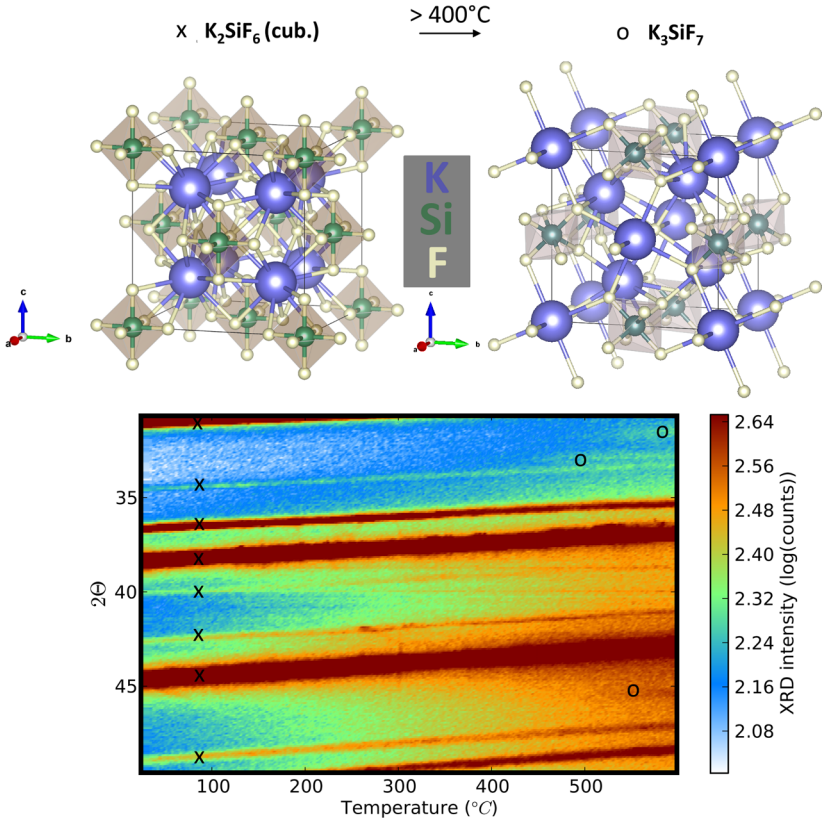

Figure 2. Top left: K_2SiF_6 structure[40] at room temperature. Top right: above 450 °C in air, the structure partially forms K_3SiF_7[42] (JCPDS: 01-073-1396). Bottom: in situ XRPD in air on commercial undoped K_2SiF_6 (JCPDS: 00-007-0217) from RT to 600 °C. The intensity scale was truncated to clarify the low-intensity peaks.

dropwise added into a Teflon or polypropylene beaker at 50 °C while stirring. Multiple synthesis parameters (mole fractions, synthesis temperature, addition rates, and precipitate recovery method) were varied in this work to optimize the purity, quantum efficiency (QE), and chemical yield. A sample list can be found in Figure S1 and Table S1 of the Supporting Information (SI), respectively, showing the X-ray powder diffraction (XRPD) patterns and relevant synthesis parameters corresponding to each sample. The best results (sample 1) were obtained from 0.33 g of K_2MnF_6 in 30 mL of HF, 7.60 g of KF in 70 mL of HF, and 3.92 g of SiO_2 in 100 mL of HF. The KF/K_2MnF_6 and SiO_2 solutions were added dropwise to each other with a rate of 56 and 68 mL/min, respectively, while stirring. After decantation, filtration, and washing with acetone, a pure K_2SiF_6:Mn^{4+} powder with a nominal concentration of 2% Mn was obtained. Complete solvent evaporation was also investigated (samples 4–7) before recovering the precipitate. However, this procedure was found to cause impurities. Scanning electron microscopy (SEM) measurements, shown in Figure 1b, reveal less defined and more brittle particles in the impure samples in comparison with the well-shaped particles of the pure sample. However, no significant difference in the average particle size (5–25 μm) was observed. The structural and chemical properties of the pure and impure samples were measured using in situ and ex situ XRPD in a Bruker D8 Advance or a Bruker D5000 diffractometer, respectively. Commercial K_2SiF_6 (>99%, Sigma-Aldrich) was used as a reference for in situ XRPD. All XRPD experiments made use of Cu Kα radiation. However, low-intensity diffraction peaks for Cu Kβ or W Lα radiation can be found in the in situ XRPD patterns due to X-ray filtering limitations. Thermogravimetric and differential thermal analysis (TGA/DTA) experiments were performed in a DTA 449 F3 Jupiter TGA/DTA system. Accelerated aging was carried out by stressing the phosphor under high-temperature and high-humidity (HTHH) conditions using a Memmert HCP 108 climate chamber. Diffuse reflectance patterns were obtained using a Varian Cary 500 spectrometer, equipped with an internal 110 mm $BaSO_4$-coated integrating sphere. Quantum efficiencies were measured using an integrating sphere (LabSphere GPS-SL series) and an EMCCD camera (Princeton Instruments ProEM 16002) connected to a spectrograph (Princeton Instruments Acton SP2358).[39] Al_2O_3 was used as the white reflective standard for these measurements. A home-built setup, consisting of a heating stage and a small vacuum chamber, was used in combination with the EMCCD camera and spectrograph to perform thermal quenching experiments from room temperature (RT) to 225 °C at a heating rate of 5 °C/min. X-ray absorption spectroscopy (XAS) at the Mn K edge was performed at the European Synchrotron Radiation Facility (ESRF) in Grenoble, France at the Dutch-Belgian (DUBBLE) beam line BM26A.

RESULTS AND DISCUSSION

Thermal and Chemical Properties of the K_2SiF_6 Host Material. The upper left part of Figure 2 shows the crystal structure of K_2SiF_6[40] at RT. The ions form a cubic lattice with the $Fm\bar{3}m$ space group. Other crystalline phases such as β-K_2SiF_6 and γ-K_2SiF_6 exist; however, they occur at high temperatures and pressures.[41] By heating in air, a partial transformation to K_3SiF_7[42] is observed above 450 °C, as can be seen in the in situ XRPD pattern of commercial K_2SiF_6 (lower part of Figure 2). Following Stodolski and Kolditz,[43,44] the onset of this transformation is caused by surface hydrolysis of K_2SiF_6 between 400 and 500 °C

$$3K_2SiF_6 + 2H_2O \rightarrow 2K_3SiF_7 + SiO_2 + 4HF\uparrow \quad (1)$$

As no SiO_2 was detected in XRPD after heating, it is concluded that the amount of SiO_2 stays below the detection limit or that the SiO_2 is mainly amorphous. In addition to surface hydrolysis, Stodolski and Kolditz[43] mentioned the bulk decomposition of

DOI: 10.1021/acsami.8b01269
ACS Appl. Mater. Interfaces 2018, 10, 18845–18856

K_2SiF_6 above 520 °C, also resulting in the formation of K_3SiF_7. The bulk decomposition is accompanied by the release of SiF_4

$$3K_2SiF_6 \rightarrow 2K_3SiF_7 + SiF_4\uparrow \quad (2)$$

Considering that the above reactions only occur at temperatures well above LED operating temperatures (which are typically below 200 °C[45]), these effects do not put any constraints on the use of K_2SiF_6 as a host material in LED phosphors. Nevertheless, impurities formed during synthesis or aging of Mn^{4+}-doped K_2SiF_6 can drastically lower the decomposition temperature of the host, as will be shown in the following.

Thermal and Chemical Properties of Pure K_2SiF_6:Mn^{4+}. A distinction will be made between inhouse samples that, as synthesized, contained impurities (designated as "impure") and samples without any impurities ("pure"). Characterization before (called "pristine") and after aging ("aged") was performed to identify the effect of impurities on the aging behavior. The in situ XRPD pattern of a pristine pure K_2SiF_6:Mn^{4+} sample (sample 1 in Figure S1 and Table S1 of the SI) is shown in Figure 3a. The powder is heated in air from RT to 600 °C. The XRPD pattern matches well with the one of undoped K_2SiF_6, indicating that the Mn dopant did not significantly modify the lattice structure as expected due to the relatively low dopant concentration (2%) and the similar ionic radii of Si^{4+} and Mn^{4+}.[46]

Upon heating, a partial transformation from K_2SiF_6 to K_3SiF_7 is observed above 450 °C due to surface hydrolysis as well as thermal bulk decomposition of K_2SiF_6. Although both compounds have a different crystal structure (Figure 2), the optical properties of Mn^{4+} are similar in both hosts. Nevertheless, a shortened decay time of the Mn^{4+} luminescence in K_3SiF_7:Mn^{4+} has been reported.[47]

To investigate its short-term stability, the pure K_2SiF_6:Mn^{4+} powder sample was placed in a climate chamber for 20 h, maintaining an atmosphere of 70 °C and 80% relative humidity (RH). Figure 3b shows the in situ XRPD measurement after aging.

For the aged material, the onset of decomposition could be expected to occur at lower temperatures compared with the pristine material, as increased hydrolysis reactions might be induced by the absorbed water. However, as the effects of aging seem rather limited in XRPD (Figure 3b) and SEM imaging (not shown), complementary techniques were used to verify this. Figure 3c,d shows the result of TGA and DTA on the pure sample before and after the aging process. The DTA result of the pristine sample indicates a relatively stable thermal behavior as no major exo- or endothermic peaks emerge during heating. Nevertheless, a weak endothermic process can be observed between 120 and 250 °C. In agreement with Stodolski and Kolditz,[43] this is ascribed to desorption processes and thermal dissociation of the surface layers, which probably also explains the mass loss of the pristine sample in the TGA experiment. As this might lead to a lowered crystallinity at the powder surface (lowering the quantum efficiency), a protective coating of the phosphor is sometimes applied.[10] After desorption and thermal dissociation, the DTA curve is flattened, after which a more pronounced exothermic degradation occurs above 520 °C. This is related to the bulk decomposition of K_2SiF_6 into K_3SiF_7 in accordance with Figure 3a, the exothermic character indicating the greater stability of K_3SiF_7 at higher temperatures. The bulk decomposition also explains the mass loss above 520 °C (seen in the TGA curve of the pristine sample) as volatile SiF_4 is

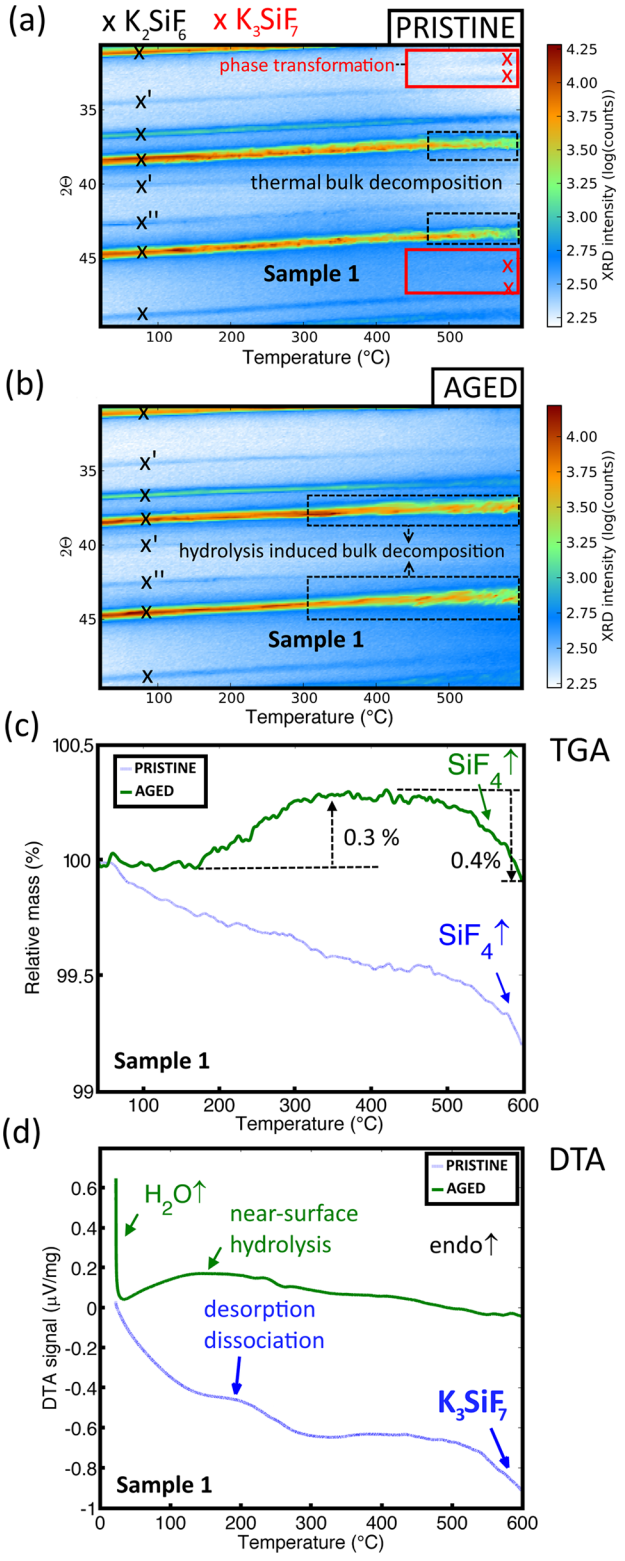

Figure 3. Chemical and structural properties of pure K_2SiF_6:Mn^{4+}. In situ XRPD pattern of pure K_2SiF_6:Mn^{4+} before (a) and after (b) aging (20 h at 70 °C/80% relative humidity (RH)). (c) Thermogravimetric analysis in dry air on the pristine and aged pure K_2SiF_6:Mn^{4+} sample. (d) Differential thermal analysis in dry air on the pristine and aged pure K_2SiF_6:Mn^{4+} sample. Next to Cu Kα, also diffraction peaks due to Cu Kβ and W Lα radiation (spurious X-ray lines present in the beam) corresponding to the same crystalline phase are present, as indicated by a single and double prime, respectively.

DOI: 10.1021/acsami.8b01269
ACS Appl. Mater. Interfaces 2018, 10, 18845−18856

released in the process. After aging at high temperature and high humidity, the thermal properties in TGA and DTA have changed. After endothermic evaporation of adsorbed water at the powder surface at slightly elevated temperatures, near-surface hydrolysis by absorbed water causes the broad endothermic feature above 30 °C (Figure 3d). In contrast to the pristine sample, the mass loss of the aged sample is negligible below 185 °C. It is expected that a small oxide buffer layer is formed during the aging process, protecting the powder surface from significant thermal dissociation and desorption.

Furthermore, the slight mass increase of 0.3% above 185 °C in the TGA curve of the aged sample suggests further oxidation at these elevated temperatures. Finally, a mass loss of 0.4% again appears due to SiF_4 release during bulk decomposition. On the basis of 2 and the molar masses of the compounds, it is estimated that a mole fraction of 3.8% K_2SiF_6 has reacted after heating to 600 °C in air to form SiF_4 and K_3SiF_7. However, the in situ XRPD of the aged sample, shown in Figure 3b, shows no diffraction peaks of K_3SiF_7. Furthermore, the exothermic behavior of the K_3SiF_7 formation is absent in the DTA curve of the aged sample. Hence, it is suspected that oxygen intake in the aged sample inhibits the crystallization of K_3SiF_7. However, as the mass loss due to SiF_4 liberation is observed in Figure 3c, we expect the K_3SiF_7 to crystallize only at temperatures above 600 °C.

Thermal and Chemical Properties of Impure K_2SiF_6:Mn^{4+}. KHF_2, a corrosive salt often found in glass etching products, is an important impurity in K_2SiF_6:Mn^{4+}. Detection of KHF_2 by XRPD is not straightforward: often, its XRPD intensities are in the same order of magnitude as the noise or even absent after decomposition of KHF_2 by moisture. Furthermore, although higher amounts of KHF_2 lead to several diffraction peaks, it is suspected that smaller amounts only lead to a single observable diffraction peak at around 2θ = 34.8°, sometimes found in the literature without further discussion.[48−50] Nevertheless, this impurity can drastically lower the stability of a phosphor sample. Figure 4a shows the in situ XRPD measurement in air on an impure K_2SiF_6:Mn^{4+} sample before aging. As can be seen, the sample contains a considerable amount of KHF_2 as an impurity phase. The in situ XRPD after aging for 20 h in a 70 °C/80% RH atmosphere is presented in Figure 4b. TGA and DTA curves on the pristine and aged impure samples are shown in Figure 4c,d, respectively. Overall comparison of Figure 4 with Figure 3 shows that the impurity induces a totally different thermal behavior of the powder. Two phases of KHF_2 have been reported:[51−53] at temperatures up to 196 °C, tetragonal KHF_2 (α-KHF_2) is favored after which it transforms to a cubic phase (β-KHF_2) before melting. The reported melting temperatures of KHF_2 range from 215 to 239 °C[51−53] and strongly depend on the exact content of KF and HF in the KF−HF system.[51] Hence, small variations in the KF/HF ratio can explain the wide variety of melting temperatures reported. For equal amounts of KF and HF, 239 °C can be considered as the accepted melting temperature.[51] Thermal decomposition of KHF_2, predominantly occurring after melting, forms KF and volatile HF.[54] However, no KF diffraction peaks are found upon heating the pristine sample above the KHF_2 melting temperature. Instead, the in situ XRPD of Figure 4a shows the crystallization of K_3SiF_7. It is suspected that the KF formed after decomposition of KHF_2 reacts with K_2SiF_6 to form K_3SiF_7. In addition to the absence of crystalline KF peaks, this would also explain the progressively lowered intensity of the diffraction peaks

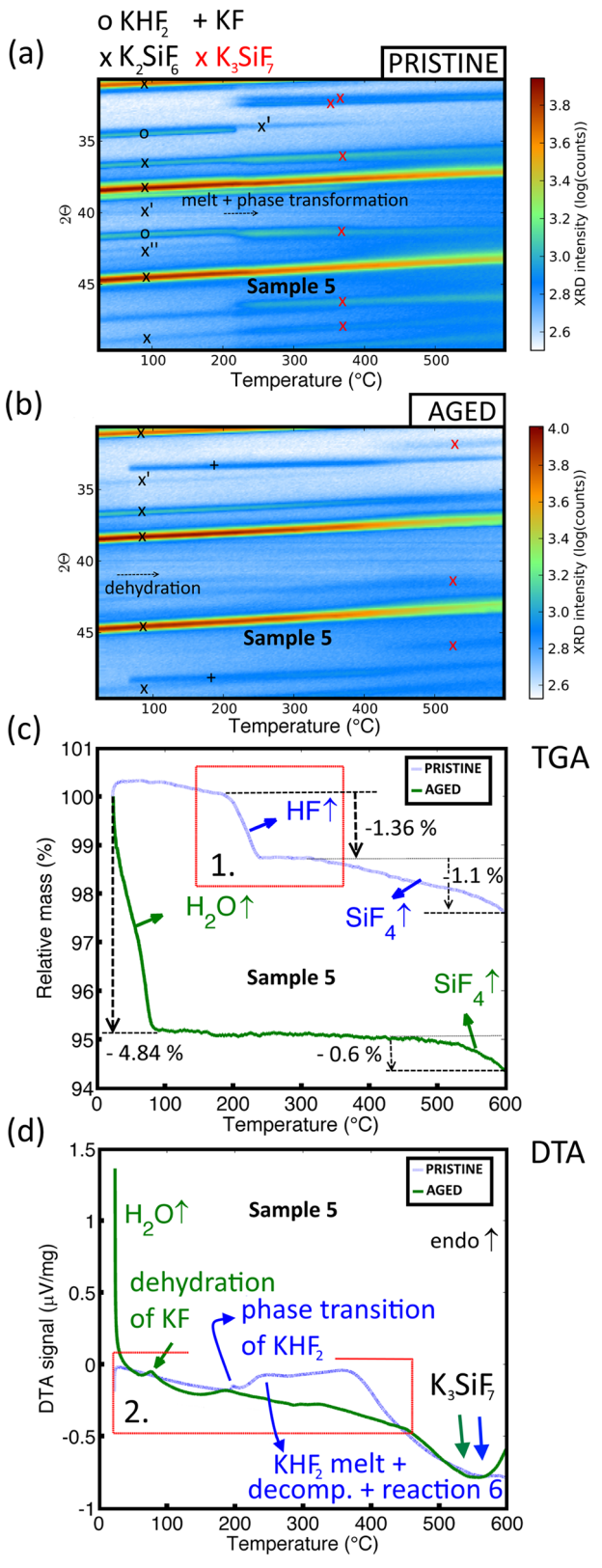

Figure 4. Chemical and structural properties of impure K_2SiF_6:Mn^{4+} in which KHF_2 (JCPDS: 00-048-1666) is present as an impurity phase. (a) In situ XRPD pattern before aging. (b) In situ XRPD pattern after aging of the sample in a 70 °C/80% RH atmosphere. (c) Thermogravimetric analysis in dry air on the pristine and aged K_2SiF_6:Mn^{4+}. (d) Differential thermal analysis in dry air on the pristine and aged K_2SiF_6:Mn^{4+}. The areas indicated by the red rectangles are shown in more detail in Figure S2 (SI).

DOI: 10.1021/acsami.8b01269
ACS Appl. Mater. Interfaces 2018, 10, 18845−18856

corresponding to K_2SiF_6. Furthermore, the formation of K_3SiF_7 is occurring at much lower temperatures than in the case of pure K_2SiF_6 host material (>450 °C) or pure K_2SiF_6:Mn^{4+}, as described in the previous sections. This confirms the findings reported before that stated that the start of K_3SiF_7 crystallization sets in earlier with increasing K excess.[43] In the DTA curve of the pristine sample, it is clear that the sample remains stable up to around 196 °C. At 196 °C, a small endothermic peak can be observed due to the $\alpha-\beta$ transition of KHF_2. This is in good agreement with the previously mentioned transition temperature.[51−53] A mass loss is observed starting at 196 °C before melting of the β-KHF_2, as visible in the TGA curve of the pristine sample in Figure 4c, which can be explained if the $\alpha-\beta$ phase transition of KHF_2 is accompanied by a partial thermal decomposition of the α-KHF_2 phase.

The KHF_2 impurity can thus cause severe damage when present in LED devices that can reach temperatures up to 200 °C. This temperature is above the $\alpha-\beta$ transition temperature of KHF_2 and close to the KHF_2 melting point. After the $\alpha-\beta$ KHF_2 phase transition, a broader endothermic peak between 220 and 280 °C is observed in the DTA curve of Figure 4d. This is ascribed to the melting and thermal decomposition of β-KHF_2 at temperatures between 220 °C (disappearance of diffraction peaks in XRPD, Figure 4a) and 239 °C (end of mass loss in TGA curve, Figure 4c).

$$KHF_2 \rightarrow KF + HF\uparrow \quad (3)$$

As soon as thermal decomposition of KHF_2 starts, K_3SiF_7 is formed by following endothermic processes[47,55]

$$K_2SiF_6 \rightarrow 2KF + SiF_4 \quad (4)$$

$$3KF + SiF_4 \rightarrow K_3SiF_7 \quad (5)$$

$$KF + K_2SiF_6 \rightarrow K_3SiF_7 \quad (6)$$

in which KHF_2 acts as the KF source. Note that 3 occurs at lower temperatures than the reported 280 °C for pure KHF_2.[54] Above 360 °C, both an exothermic process and a mass loss are observed which are both attributed to the $K_2SiF_6 \rightarrow K_3SiF_7$ bulk decomposition, releasing SiF_4. The effect of aging on the impure powder is shown in Figure 4b. The aged sample is unstable even at low temperatures as crystalline KF is formed around 60 °C. The large mass loss of the aged sample below 80 °C, shown in Figure 4c, can be explained by the evaporation of water. The formation of KF is thus likely preceded by a dehydration process. Therefore, it is suspected that KHF_2, present before aging in the pristine impure sample, is decomposed during the aging process, forming hydrated KF and releasing HF. This explains the disappearance of the KHF_2 diffraction peaks after aging in impure samples, as seen in Figure 5. The hydrated KF can lose its water upon heating, explaining the mass loss in TGA and the appearance of the diffraction peaks corresponding to anhydrous KF in Figure 4b. KF is known to form two hydrated states: $KF\cdot(H_2O)_2$ and $KF\cdot(H_2O)_4$.[56] Decomposition of KHF_2 and subsequent hydration of KF during aging of the sample can hence be described as

$$KHF_2 + nH_2O \rightarrow KF\cdot(H_2O)_n + HF\uparrow \quad (7)$$

in which n equals 2 or 4.[56]

A value of $n = 4$ could provide enough water molecules to explain the observed mass loss of around 4.8 mass % in the TGA curve of the aged sample in Figure 4c. Thereby, it is assumed that a content of 5.30 mass % of KHF_2 impurity in the pristine sample was fully decomposed during the aging process, forming hydrated KF. Furthermore, it was assumed the hydrate is the only significant water-containing species in the aged sample (see the SI). As the mass loss in the TGA curve of the aged sample in Figure 4c consists of two slopes, it is probable that $KF\cdot(H_2O)_4$ first partially dehydrates to $KF\cdot(H_2O)_2$ before forming anhydrous KF. This could explain the presence of a small diffraction peak at around $2\theta = 30°$ in some of the aged samples (Figure S3 in the SI). After dehydration, anhydrous crystalline KF is left behind, as confirmed by XRPD in Figure 4b. The crystal water loss also explains the initial steep drop in the DTA curve of the aged sample in Figure 4d similar to the drop in the pure aged sample. Hence, hydrated KF might also be present in the latter, although no evidence was found with in situ XRPD. In the impure sample, the KF formed by dehydration is relatively stable at high temperatures, as can be seen in Figure 4b. This is in contrast to the KF that was formed in the decomposition of KHF_2 (3) during thermal treatment of the pristine sample. Only at the highest temperatures, part of the dehydrated KF is consumed together with K_2SiF_6 to form K_3SiF_7. This occurs in addition to the bulk decomposition reaction which liberates SiF_4, explaining again the mass loss and endothermic behavior observed above 500 °C in Figure 4c.

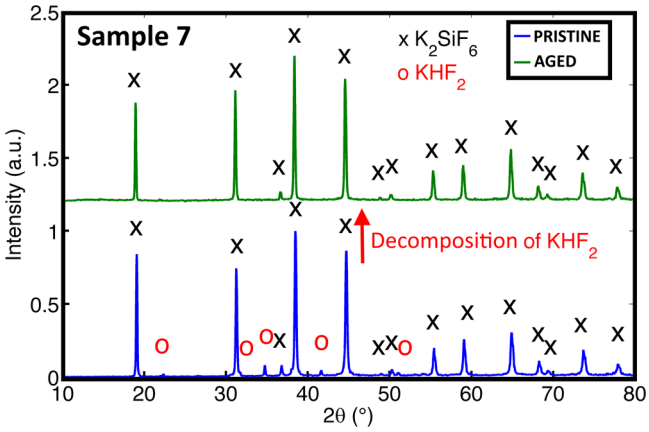

Figure 5. Effect of aging on the KHF_2 impurity. No impurity diffraction peaks are observed after aging due to decomposition of KHF_2 by moisture. The cross symbols indicate K_2SiF_6 (JCPDS: 00-007-0217) while the circles indicate KHF_2 (JCPDS: 00-048-1666).

Optical Properties of Pure and Impure K_2SiF_6:Mn^{4+}. Figure 6a shows the XRPD patterns of one pure sample (sample 1) and two impure samples (samples 4 and 7), all before aging. The diffuse reflectance spectra before and after aging in a 70 °C/80% RH atmosphere of the pure sample are shown in Figure 6b. The pure powder had to be aged for at least 48 h to observe a change in its diffuse reflection pattern in contrast with the samples containing KHF_2 that showed drastic differences after only 20 h of aging (Figure 6c). For the pure sample, two absorption bands are present at around 345 and 450 nm (Figure 6b), which correspond to the $^4A_{2g} \rightarrow {}^4T_{1g}$ and $^4A_{2g} \rightarrow {}^4T_{2g}$ electronic transitions of Mn^{4+} in $[MnF_6]^{2-}$, respectively.[36,57] No unexpected absorption bands are observed. However, the diffuse reflectance patterns of the impure powders (Figure 6c) show an additional (parasitic) absorption superposed at the long wavelength side of the 450 nm band. Also in other reports, a part of this parasitic absorption (500−620 nm) can be seen, most often without any further discussion.[58−63]

DOI: 10.1021/acsami.8b01269
ACS Appl. Mater. Interfaces 2018, 10, 18845−18856

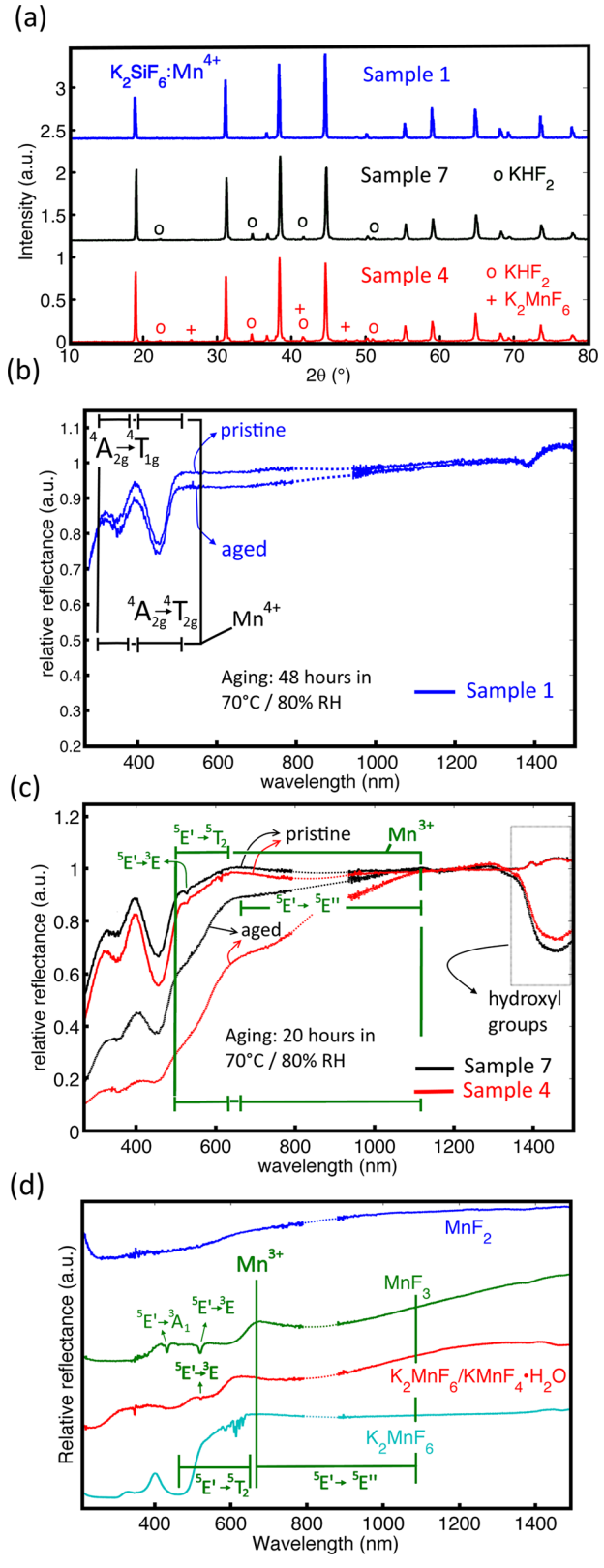

Figure 6. (a) XRPD patterns of pure and impure K_2SiF_6:Mn^{4+} (b) Diffuse reflectance pattern of a pure K_2SiF_6:Mn^{4+} sample before and after aging (48 h). The dashed line is a guide to the eye in the region where the detector is switched. (c) Diffuse reflectance pattern of K_2SiF_6:Mn^{4+} samples with KHF_2 impurity, before and after aging (24 h). Sample 4 also contained K_2MnF_6 as an impurity. (d) Diffuse reflectance on fluoride samples used as a reference.

Murphy et al.[12] reported a similar parasitic absorption in untreated K_2SiF_6:Mn^{4+} after aging in a 85 °C/85% RH atmosphere, causing brown discoloration of the powder. They ascribed the parasitic absorption to Mn species, produced after hydrolysis of near-surface/surface $[MnF_6]^{2-}$ groups, containing mixed Mn valence states.

In this work, the parasitic absorption between 500 and 620 nm in both pristine and aged K_2SiF_6:Mn^{4+} samples as well as the broad absorption centered around 800 nm (both indicated by the green rectangle of Figure 6c) is attributed to Mn^{3+}. This assignment is based on comparison of the samples with the diffuse reflectance of several fluoride references containing Mn^{4+}, Mn^{3+}, and Mn^{2+}. Figure 6d displays the diffuse reflectance spectra of K_2MnF_6, $KMnF_4{\cdot}H_2O$ (containing traces of K_2MnF_6, see Figure S4 in the SI), MnF_3, and MnF_2, showing that an absorption similar to the one in the green rectangle of Figure 6c can be observed in MnF_3 and $KMnF_4{\cdot}H_2O$. In contrast to Mn^{4+} and Mn^{2+}, the trivalent state of manganese, Mn^{3+}, is seldom encountered in the luminescence literature.

Mostly, it does not exhibit radiative decay due to a strong Jahn−Teller effect, facilitating multiphonon decay of the excited states.[64] In some cases, infrared emission is possible.[65,66] In any case, the Mn^{3+} ion has characteristic absorption features due to crystal field transitions within the $3d^4$ configuration. Broad absorption bands are expected in the deep red/near-IR and the green-yellow range of the spectrum due to spin-allowed transitions, the former to be between the Jahn−Teller split ^5E ground state (denoted as $^5E' \rightarrow {}^5E''$), the latter to be from the $^5E'$ ground state to the $^5T_2$ excited state. In addition to these broad absorption bands, sharp and less intense features due to spin-forbidden transitions ($^5E' \rightarrow {}^3E$ and $^5E' \rightarrow {}^3A_1$) can sometimes also be found.[67]

It is clear that the sharp absorption feature around 518 nm can be attributed to the $^5E' \rightarrow {}^3E$ spin flip transition of Mn^{3+} in MnF_3. A similar absorption line can be found in $KMnF_4{\cdot}H_2O$ and the K_2SiF_6:Mn^{4+} samples of Figure 6c as well. In addition to this absorption line, also broad absorption bands due to the presence of Mn^{3+} can be identified in the reflectance spectra. The $^5E' \rightarrow {}^5T_2$ transition occurs in fluorides as a broad and intense absorption band between roughly 410 and 620 nm. Especially, the low-energy side of this band is visible in the MnF_3 reflectance spectrum. Comparing the spectra of the pure (Figure 6b) to those of the impure K_2SiF_6:Mn^{4+} (Figure 6c) powders, one learns that this Mn^{3+} $^5E' \rightarrow {}^5T_2$ absorption band occurs as a broad shoulder at the low-energy side of the expected Mn^{4+} $^4A_{2g} \rightarrow {}^4T_{2g}$ absorption band. Because of the high oscillator strength of this spin-allowed Mn^{3+} absorption band, its presence or absence can be used to detect unintended Mn^{3+} species in as-prepared fluoride phosphors. At lower energies, even the $^5E' \rightarrow {}^5E''$ Jahn−Teller transition of Mn^{3+} can be observed in the impure samples as a broad dip in the reflectance ranging from 650 to 1100 nm. As Mn^{3+} impurity ions lead to parasitic absorption in K_2SiF_6:Mn^{4+}, followed by nonradiative decay, their presence will lead to a lowered quantum efficiency of the impure phosphor.

In pristine K_2SiF_6:Mn^{4+}, the presence of Mn^{3+} can be explained by an insufficient control of the synthesis parameters. First, during K_2MnF_6 precursor synthesis, Mn^{3+} can be formed due to parasitic synthesis reactions when the manganese reduction is poorly controlled.[68] This is evidenced by the Mn^{3+} $^5E' \rightarrow {}^5T_2$ optical absorption in the K_2MnF_6 diffuse reflectance spectrum of Figure 6d between 500 and 620 nm. Moreover, in K_2MnF_6 samples with a more pronounced Mn^{3+} absorption,

DOI: 10.1021/acsami.8b01269
ACS Appl. Mater. Interfaces 2018, 10, 18845−18856

XRPD revealed the presence of a Mn^{3+}-hydrate: $K_2MnF_5{\cdot}H_2O$ (Figure S5 in the SI). The hydrate can form during precursor synthesis due to following reaction[69]

$$KMnO_4 + KF + 4HF + 2H_2O_2 \rightarrow K_2MnF_5{\cdot}H_2O + 3H_2O + 2O_2\uparrow \quad (8)$$

In $K_2MnF_5{\cdot}H_2O$, the crystal water does not contribute to the first coordination sphere of the Mn ions. This differs from a second type of Mn^{3+}-hydrate formation which occurs when K_2MnF_6 is dissolved in heated HF solutions, as is the case during the second synthesis step of fluoride phosphors.[23,26,62,70] While dissolving K_2MnF_6 (containing the $K_2MnF_5{\cdot}H_2O$ impurity) in heated HF solutions, dissociation occurs, after which $[MnF_6]^{2-}$ complexes can be partially hydrolyzed and hydrated at a rate depending on the solution temperature. Subsequent addition of acetone as a nonsolvent leads to precipitation of $KMnF_4{\cdot}H_2O$. In contrast to $K_2MnF_5{\cdot}H_2O$, the crystal water in $KMnF_4{\cdot}H_2O$ now contributes to the first coordination sphere of the Mn ions.[68] It is thus expected that during the first and second step of the K_2SiF_6:Mn^{4+} synthesis, hydrolysis and hydration processes can lead to the presence of hydrated Mn^{3+}-containing structures in addition to K_2SiF_6:Mn^{4+}.

Techniques that are sensitive to the first coordination sphere of Mn, such as X-ray absorption spectroscopy, might discriminate between both types of Mn^{3+} species.[71] X-ray absorption near-edge spectroscopy (XANES) was performed at the Mn K edge on four K_2SiF_6:Mn^{4+} samples with different Mn concentrations of 1.7, 3.9, 7.3, and 10.8% (samples 4−7 in the SI), all synthesized using the same K_2MnF_6 precursor. The XANES results are shown in Figure S6 of the SI. In Figure 7, only the results for the sample with the highest doping concentration are shown for clarity. Similar results were obtained at lower doping concentrations (Figure S6). The position of the absolute maxima in the K_2SiF_6:Mn^{4+} first derivative XANES spectra (Figures 7 and S6) matches well with the Mn^{4+} Kα edge energy in K_2MnF_6, which is taken as the Mn^{4+} reference here.[68] However, a broadening on the low-energy side is found that is caused by the existence of lower Mn valences, presumably Mn^{3+}, as shown by our optical absorption experiment. Comparison of the K_2SiF_6:Mn^{4+} XANES spectra with the XANES spectra of fluoride or oxide references provides a tool to discriminate between fluorine or oxygen coordination for the Mn^{3+}. All investigated K_2SiF_6:Mn^{4+} samples show a low-energy sideband coinciding with the MnF_3 reference (Figure 7) except for the sample with the lowest Mn concentration in which the sideband matches better with the Mn_2O_3 reference (Figure S6 in the SI). This further confirms the occurrence of Mn^{3+}, as expected from the diffuse reflectance patterns (Figure 6).

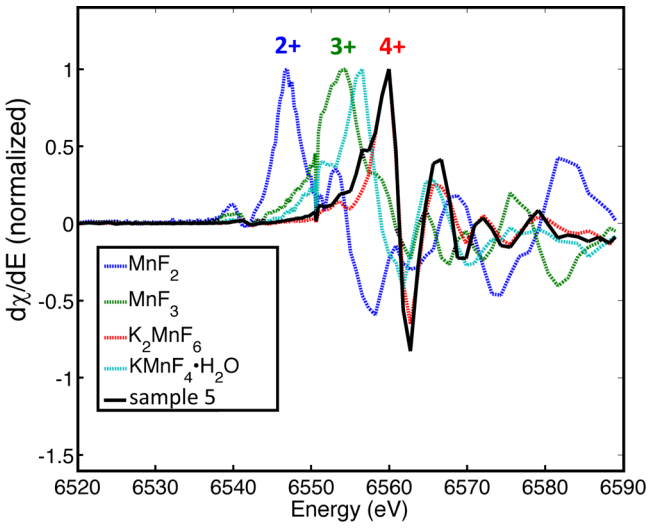

Figure 7. First derivative of the Mn K edge XANES spectra of Mn^{2+}, Mn^{3+}, and Mn^{4+} fluorides and Mn^{3+} in a hydrated fluoride ($KMnF_4{\cdot}H_2O$). The black curve corresponds to an impure K_2SiF_6:Mn^{4+} sample (sample 5) containing KHF_2 as a crystalline impurity. The latter contains contributions of Mn^{4+} and Mn^{3+} in metal−aqua complexes as well as fluorine coordination.

Apart from the bands related to Mn^{3+} in pure oxygen or fluorine coordination, the XANES results indicate an additional type of coordination for the Mn^{3+} ions. An additional shoulder band, coinciding with the main edge peak in the first derivative XANES spectrum of $KMnF_4{\cdot}H_2O$, is sometimes observed (Figures 7 and S6 in the SI). Upon inspection of the XANES spectrum for $KMnF_4{\cdot}H_2O$ (the cyan curve in Figure 7), it seems that the maximum of the derivative does not coincide with the maximum for MnF_3 but is slightly shifted to higher energies. This edge shift is probably due to water molecules in the first coordination shell that bind in a less ionic way to the Mn ion.[71] Hence, K_2SiF_6:Mn^{4+} samples for which the XANES spectra contain the additional shoulder band are expected to contain hydrated Mn^{3+}-containing structures such as $KMnF_4{\cdot}H_2O$ in which H_2O molecules take the place of fluorine in the first coordination shell of Mn. As this shoulder band was not found in the K_2MnF_6 reference, the XANES results confirm that the hydrated Mn^{3+} centers are formed during the second synthesis step, after dissolving K_2MnF_6 in a heated (50 °C) solution of 40% HF. In $K_2MnF_5{\cdot}H_2O$, all Mn ions are fully coordinated by fluorine ligands, explaining why only the MnF_3 reference spectrum resembles the shoulder band in K_2MnF_6. Formation of $KMnF_4{\cdot}H_2O$ seems to preferentially occur at temperatures higher than the 0 °C during synthesis of the precursor.

Considering the first derivative XANES spectra and the XRPD patterns of the concentration series (Figures S6 and S7), an increased amount of KHF_2 and $KMnF_4{\cdot}H_2O$ can possibly be linked to an increased Mn concentration. As more precursor material is needed with higher doping concentrations, more of the K_2MnF_6 and $K_2MnF_5{\cdot}H_2O$ impurity reacts in the heated 40% HF solution to form $KMnF_4{\cdot}H_2O$ and KHF_2. K_2MnF_6 quickly reacts in 40% HF at elevated temperatures. From these solutions, $KMnF_4{\cdot}H_2O$ precipitated after acetone addition.[68] However, when K_2MnF_6 is dissolved in demineralized water at 95 °C, $K_2MnF_5{\cdot}H_2O$, KHF_2, and possibly MnO_2 and $KMnO_4$ are formed after evaporation of the solvent, as verified by ex situ XRD on the brown-colored precipitate (Figure S4). Therefore, we propose following reactions to occur in heated 40% HF solutions

$$4K_2MnF_6 + 7H_2O \rightarrow 3K_2MnF_5{\cdot}H_2O + KHF_2 + 7HF + KMnO_4 \quad (9)$$

$$K_2MnF_5{\cdot}H_2O + HF \rightarrow KMnF_4{\cdot}H_2O + KHF_2 \quad (10)$$

$$K_2MnF_6 + 2\,H_2O \rightarrow 2KHF_2 + 2HF + MnO_2 \quad (11)$$

DOI: 10.1021/acsami.8b01269
ACS Appl. Mater. Interfaces 2018, 10, 18845−18856

Figure S7b,c shows that although the absorption at 450 nm excitation is increased upon increasing the Mn concentration, the internal and external quantum efficiency values (IQE and EQE) decrease. On one hand, this can be explained by the increase of the Mn^{3+} species that are absorbing excitation light but decay nonradiatively. On the other hand, traces of the K_2MnF_6 precursor were found in the samples with a Mn concentration of 7.3 and 10.8%, which is expected to increase the Mn absorption while decreasing the radiative decay due to concentration quenching in the K_2MnF_6 impurities.

As the KHF_2 impurity affects the chemical stability of the phosphor (Thermal and Chemical Properties of Impure K2SiF6:Mn4+), this impurity also negatively influences the optical properties of an impure powder after ageing. As mentioned before, a high stability was found for the pure sample, which did not show a significant change in diffuse reflectance after 48 h of aging (Figure 6b). However, a drastic change in the diffuse reflectance was found for the impure samples after only 20 h of aging (Figure 6c). There, the increased optical absorption at around 1400 nm might be explained by hydroxyl groups after water absorption[72,73] (see Figure S8 in the SI). The absorbed water decomposes the KHF_2, forming hydrated KF and HF, which can trigger the formation of Mn^{3+} species that cause increased parasitic absorption after aging (Figure 6c). It is clear that drastic improvements of the chemical stability are obtained by avoiding any KHF_2 formation during synthesis. It is suspected that at any time during the synthesis, an excess of KF and K_2MnF_6 relative to SiO_2 can cause partial precipitation of KHF_2 due to interaction of KF with HF or by means of 9−11.

Nevertheless, it was found that KHF_2 precipitation can be suppressed by using an appropriate drop rate of the KF/K_2MnF_6 and SiO_2 solutions and using decantation and filtration before considerable evaporation of the solvent occurs. In contrast to complete solvent evaporation (sample 4−7), this leads to pure K_2SiF_6:Mn^{4+} (sample 1) without KHF_2 or Mn^{3+} impurities.

Besides the chemical stability, thermal quenching was also evaluated. Figure 8 shows the thermal quenching of an impure (sample 6) and a pure K_2SiF_6:Mn^{4+} sample (sample 1) with an equal nominal Mn concentration of 2 atom %. A slight enhancement of the photoluminescence (PL) intensity up to 120 °C is found for the impure sample, whereas a more pronounced increase of intensity from RT to 150 °C is found for the pure sample (which is an improvement if compared with previously reported values of up to 140 °C[74−76]). The enhancement of the PL intensity has been linked to the increase of phonon-assisted radiative transitions with increasing temperature.[75] The high purity of sample 1 also explains the enhanced internal and external quantum efficiency values (EQE = 32%, IQE 96%) compared with the values obtained for the impure sample 6 (EQE = 14%, IQE = 53%). The absence of secondary Mn valences in sample 1 prevents parasitic absorption of the excitation light, which would lead to low IQE values, as the case in sample 6. Absence of impurity phases such as KHF_2 is responsible for the high chemical stability of sample 1. Both types of impurities should thus be monitored and avoided to obtain phosphors with high IQE, EQE, as well as high chemical and thermal stability.

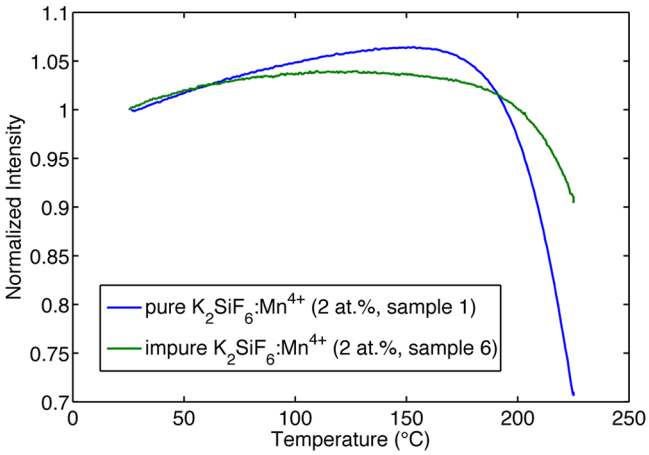

Figure 8. Thermal quenching curves of the integrated luminescence of pure (sample 1) and impure (sample 6) K_2SiF_6:Mn^{4+}. Excitation was performed using a blue (450 nm) LED.

CONCLUSIONS

The stability of K_2SiF_6:Mn^{4+} phosphor was investigated as a function of synthesis conditions and the occurrence of unwanted impurities. The K_2SiF_6 host proves to be chemically stable at LED operating temperatures (<200 °C) and elevated humidity levels. However, at temperatures above 400 °C, effects of surface hydrolysis and bulk decomposition can be observed, as was demonstrated by in situ XRPD. In both processes, K_2SiF_6 partially transforms to K_3SiF_7 with the release of HF in the former and SiF_4 in the latter, confirming the work done by Stodolski and Kolditz.[43] Doping the host material with Mn^{4+} requires the use of wet chemical synthesis methods, with the risk of impurity formation in the form of KHF_2 and Mn^{3+} hydrates, such as $K_2MnF_5{\cdot}H_2O$ and $KMnF_4{\cdot}H_2O$. It was found that the impurities severely affect the chemical stability and optical performance of the phosphor. Interaction of KHF_2 with K_2SiF_6 leads to K_3SiF_7 formation at temperatures above 196 °C. Furthermore, when impure phosphor material is in contact with moisture in a high-temperature and high-humidity atmosphere, the KHF_2 impurity forms hydrated KF and HF. The KF hydrate is amorphous at RT and hence cannot be detected straightforward in XRPD. Dehydration occurs at only 60 °C, forming anhydrous KF, as verified by TGA and in situ XRPD. Impure powders that, as synthesized, contain KHF_2 and Mn^{3+} hydrate impurities, show an increased contribution of Mn^{3+} and hydroxyl groups in the optical absorption after aging under high-temperature and high-humidity conditions. It is therefore concluded that Mn^{3+} species are easily formed during the aging process of these impure powders. Control of the addition rate of precursor materials and appropriate recovery of the phosphor precipitate proves crucial in minimizing impurity formation. It was found that complete evaporation of the solvent led to impure phosphor whereas decantation, filtration, and washing led to impurity-free fluoride phosphors with high QE and chemical and thermal stability. Although the current work focuses on the effect of impurities on the short-term stability of K_2SiF_6:Mn^{4+} at high-temperature and high-humidity conditions, follow up research is needed to carefully evaluate the influence of long term exposure to high irradiances in combination with high temperatures and high humidity.

ASSOCIATED CONTENT

Supporting Information

The Supporting Information is available free of charge on the ACS Publications website at DOI: 10.1021/acsami.8b01269.

DOI: 10.1021/acsami.8b01269
ACS Appl. Mater. Interfaces 2018, 10, 18845−18856

$K_2SiF_6:Mn^{4+}$ samples; decomposition of KHF_2 by moisture and formation of the KF hydrate; XRPD pattern of Mn^{3+}-hydrate impurities; diffuse reflection on K_2MnF_6 precursor material; XANES analysis and optical properties of the concentration series; diffuse reflectance on $K_2SiF_6:Mn^{4+}$ and $KMnF_4·H_2O$ (PDF)

AUTHOR INFORMATION

Corresponding Author

*E-mail: Philippe.Smet@UGent.be.

ORCID

Reinert Verstraete: 0000-0003-1914-5456
Heleen F. Sijbom: 0000-0001-6565-9859
Jonas J. Joos: 0000-0002-7869-2217
Philippe F. Smet: 0000-0003-4789-5799

Funding

R.V., H.F.S., J.J.J., K.K., D.P., and P.F.S. thank the agency for Innovation by Science and Technology (IWT) for a SBO-IWT grant (SBO130030), the National Research Foundation (NRF) and the Research Foundation Flanders (FWO) for their grant (joint FWO-NRF project, project number: G0H0417N). J.J.J. thanks the UGent Special Research Fund (BOF) for a postdoctoral grant.

Notes

The authors declare no competing financial interest.

ACKNOWLEDGMENTS

Our gratitude goes to the Department of Chemistry of Ghent University for the use of the TGA/DTA setup and the staff and infrastructure at the DUBBLE beam line, ESRF, Grenoble, France.

REFERENCES

(1) Jiang, S.; Yamamoto, H.; Digonnet, M. J. F.; Glesener, J. W.; Dries, J. C. In *White LED Phosphors: the Next Step*, Proceedings of the Optical Components and Materials VII, 2010; Vol. *7598*, 759808.

(2) Smet, P. F.; Parmentier, A. B.; Poelman, D. Selecting Conversion Phosphors for White Light-Emitting Diodes. *J. Electrochem. Soc.* **2011**, *158*, R37−R54.

(3) Tsai, C. C.; Wang, J.; Chen, M. H.; Hsu, Y. C.; Lin, Y. J.; Lee, C. W.; Huang, S. B.; Hu, H. L.; Cheng, W. H. Investigation of Ce:YAG Doping Effect on Thermal Aging for High-Power Phosphor-Converted White-Light-Emitting Diodes. *IEEE Trans. Device Mater. Reliab.* **2009**, *9*, 367−371.

(4) Ye, S.; Xiao, F.; Pan, Y. X.; Ma, Y. Y.; Zhang, Q. Y. Phosphors in Phosphor-converted White Light-emitting Diodes: Recent Advances in Materials, Techniques and Properties. *Mater. Sci. Eng., R* **2010**, *71*, 1−34.

(5) Shi, H.; Zhu, C.; Huang, J.; Chen, J.; Chen, D.; Wang, W.; Wang, F.; Cao, Y.; Yuan, X. Luminescence Properties of YAG:Ce, Gd Phosphors Synthesized Under Vacuum Condition and Their White LED Performances. *Opt. Mater. Express* **2014**, *4*, 649−655.

(6) Lin, C. C.; Meijerink, A.; Liu, R. S. Critical Red Components for Next-Generation White LEDs. *J. Phys. Chem. Lett.* **2016**, *7*, 495−503.

(7) Union, I. T. *ITU-R BT.2020: Parameter Values for Ultra-High Definition Television Systems for Production and International Programme Exchange*; International Telecommunication Union, 2012.

(8) Abe, S.; Joos, J. J.; Martin, L. I. D. J.; Hens, Z.; Smet, P. F. Hybrid Remote Quantum Dot/Powder Phosphor Designs for Display Backlights. *Light: Sci. Appl.* **2017**, *6*, No. e16271.

(9) Hoshino, R.; Adachi, S. Photo-induced Degradation and Thermal Decomposition in $ZnSnF_6·6H_2O:Mn^{4+}$ Red-emitting Phosphor. *Opt. Mater.* **2015**, *48*, 36−43.

(10) Nguyen, H. D.; Lin, C. C.; Liu, R. S. Waterproof Alkyl Phosphate Coated Fluoride Phosphors for Optoelectronic Materials. *Angew. Chem., Int. Ed.* **2015**, *54*, 10862−10866.

(11) Zhou, Y. Y.; Song, E. H.; Deng, T. T.; Zhang, Q. Y. Waterproof Narrow-Band Fluoride Red Phosphor $K_2TiF_6:Mn^{4+}$ via Facile Superhydrophobic Surface Modification. *ACS Appl. Mater. Interfaces* **2018**, *10*, 880−889.

(12) Murphy, J. E.; Garcia-Santamaria, F.; Setlur, A. A.; Sista, S. PFS, $K_2SiF_6:Mn^{4+}$: the Red-line Emitting LED Phosphor behind GE's TriGain Technology Platform. *SID Symp. Dig. Tech. Pap.* **2015**, *46*, 927−930.

(13) Singh, P.; Tan, C. M. Degradation Physics of High Power LEDs in Outdoor Environment and the Role of Phosphor in the Degradation Process. *Sci. Rep.* **2016**, *6*, No. 24052.

(14) Smet, P. F.; Joos, J. J. White Light-emitting Diodes: Stabilizing Colour and Intensity. *Nat. Mater.* **2017**, *16*, 500−501.

(15) Hu, Y.; Zhuang, W.; Ye, H.; Zhang, S.; Fang, Y.; Huang, X. Preparation and Luminescent Properties of $(Ca_{1-x}Sr_x)S:Eu^{2+}$ Red-emitting Phosphor for White LED. *J. Lumin.* **2005**, *111*, 139−145.

(16) Avci, N.; Cimieri, I.; Smet, P. F.; Poelman, D. Stability Improvement of Moisture Sensitive $CaS:Eu^{2+}$ Micro-particles by Coating with Sol−gel Alumina. *Opt. Mater.* **2011**, *33*, 1032−1035.

(17) Piao, X.; Machida, K.; Horikawa, T.; Hanzawa, H.; Shimomura, Y.; Kijima, N. Preparation of $CaAlSiN_3:Eu^{2+}$ Phosphors by the Self-propagating High-temperature Synthesis and their Luminescent Properties. *Chem. Mater.* **2007**, *19*, 4592−4599.

(18) Li, Y. Q.; van Steen, J. E. J.; van Krevel, J. W. H.; Botty, G.; Delsing, A. C. A.; DiSalvo, F. J.; de With, G.; Hintzen, H. T. Luminescence Properties of Red-emitting $M_2Si_5N_8:Eu^{2+}$ (M = Ca, Sr, Ba) LED Conversion Phosphors. *J. Alloys Compd.* **2006**, *417*, 273−279.

(19) Pust, P.; Weiler, V.; Hecht, C.; Tucks, A.; Wochnik, A. S.; Henss, A. K.; Wiechert, D.; Scheu, C.; Schmidt, P. J.; Schnick, W. Narrow-band Red-emitting $Sr[LiAl_3N_4]:Eu^{2+}$ as a Next-generation LED-phosphor Material. *Nat. Mater.* **2014**, *13*, 891−896.

(20) Moon, J. W.; Min, B. G.; Kim, J. S.; Jang, M. S.; Ok, K. M.; Han, K.-Y.; Yoo, J. S. Optical Characteristics and Longevity of the Line-emitting $K_2SiF_6:Mn^{4+}$ Phosphor for LED Application. *Opt. Mater. Express* **2016**, *6*, 782−792.

(21) Jiang, X. Y.; Pan, Y. X.; Huang, S. M.; Chen, X.; Wang, J. G.; Liu, G. K. Hydrothermal Synthesis and Photoluminescence Properties of Red Phosphor $BaSiF_6:Mn^{4+}$ for LED Applications. *J. Mater. Chem. C* **2014**, *2*, 2301−2306.

(22) Adachi, S.; Abe, H.; Kasa, R.; Arai, T. Synthesis and Properties of Hetero-Dialkaline Hexafluorosilicate Red Phosphor $KNaSiF_6:Mn^{4+}$. *J. Electrochem. Soc.* **2012**, *159*, J34−J37.

(23) Du, M.; Tang, F.; Long, J.; Ma, C.; Yuan, X.; Zhang, J.; Wen, Z.; Ma, R.; Cao, Y. Optical and Thermal Behaviors of High Efficient $K_2TiF_6:Mn^{4+}$ Red Phosphor Prepared by Modified Two-step Co-precipitation Method. *Mater. Res. Bull.* **2016**, *83*, 316−323.

(24) Zhu, H.; Lin, C. C.; Luo, W.; Shu, S.; Liu, Z.; Liu, Y.; Kong, J.; Ma, E.; Cao, Y.; Liu, R. S.; Chen, X. Highly Efficient Non-rare-earth Red Emitting Phosphor for Warm White Light-emitting Diodes. *Nat. Commun.* **2014**, *5*, No. 4312.

(25) Zhou, Q.; Tan, H. Y.; Zhou, Y. Y.; Zhang, Q. H.; Wang, Z. L.; Yan, J.; Wu, M. M. Optical Performance of Mn^{4+} in a New Hexa-coordinated Fluorozirconate Complex of Cs_2ZrF_6. *J. Mater. Chem. C* **2016**, *4*, 7443−7448.

(26) Zhou, Q.; Zhou, Y. Y.; Liu, Y.; Wang, Z. L.; Chen, G.; Peng, J. H.; Yan, J.; Wu, M. M. A New and Efficient Red Phosphor for Solid-state Lighting: $Cs_2TiF_6:Mn^{4+}$. *J. Mater. Chem. C* **2015**, *3*, 9615−9619.

(27) Adachi, S.; Takahashi, T. Photoluminescent Properties of $K_2GeF_6:Mn^{4+}$ Red Phosphor Synthesized from Aqueous $HF/KMnO_4$ Solution. *J. Appl. Phys.* **2009**, *106*, No. 013516.

(28) Xu, Y. K.; Adachi, S. Properties of $Na_2SiF_6:Mn^{4+}$ and $Na_2GeF_6:Mn^{4+}$ Red Phosphors Synthesized by Wet Chemical Etching. *J. Appl. Phys.* **2009**, *105*, No. 013525.

DOI: 10.1021/acsami.8b01269
ACS Appl. Mater. Interfaces 2018, 10, 18845−18856

(29) Hoshino, R.; Nakamura, T.; Adachi, S. Synthesis and Photoluminescence Properties of $BaSnF_6$:Mn^{4+} Red Phosphor. *ECS J. Solid State Sci. Technol.* **2016**, *5*, R37−R43.
(30) Sekiguchi, D.; Adachi, S. Synthesis and Photoluminescence Spectroscopy of $BaGeF_6$:Mn^{4+} Red Phosphor. *Opt. Mater.* **2015**, *42*, 417−422.
(31) Xu, Y. K.; Adachi, S. Properties of Mn^{4+}-Activated Hexafluorotitanate Phosphors. *J. Electrochem. Soc.* **2011**, *158*, J58−J65.
(32) Senden, T.; van Harten, E. J.; Meijerink, A. Synthesis and Narrow Red Luminescence of Cs_2HfF_6:Mn^{4+}, a New Phosphor for Warm White LEDs. *J. Lumin.* **2018**, *194*, 131−138.
(33) Kasa, R.; Adachi, S. Mn-activated K_2ZrF_6 and Na_2ZrF_6 Phosphors: Sharp Red and Oscillatory Blue-green Emissions. *J. Appl. Phys.* **2012**, *112*, No. 013506.
(34) Jin, Y.; Fang, M. H.; Grinberg, M.; Mahlik, S.; Lesniewski, T.; Brik, M. G.; Luo, G. Y.; Lin, J. G.; Liu, R. S. Narrow Red Emission Band Fluoride Phosphor $KNaSiF_6$:Mn^{4+} for Warm White Light-Emitting Diodes. *ACS Appl. Mater. Interfaces* **2016**, *8*, 11194−11203.
(35) Sijbom, H. F.; Verstraete, R.; Joos, J. J.; Poelman, D.; Smet, P. F. K_2SiF_6:Mn^{4+} as a Red Phosphor for Displays and Warm-white LEDs: a Review of Properties and Perspectives. *Opt. Mater. Express* **2017**, *7*, 3332−3365.
(36) Sijbom, H. F.; Joos, J. J.; Martin, L. I. D. J.; Van den Eeckhout, K.; Poelman, D.; Smet, P. F. Luminescent Behavior of the K_2SiF_6:Mn^{4+} Red Phosphor at High Fluxes and at the Microscopic Level. *ECS J. Solid State Sci. Technol.* **2016**, *5*, R3040−R3048.
(37) Garcia-Santamaria, F.; Murphy, J. E.; Setlur, A. A.; Sista, S. P. Concentration Quenching in K_2SiF_6:Mn^{4+} Phosphors. *ECS J. Solid State Sci. Technol.* **2018**, *7*, R3030−R3033.
(38) Bode, H.; Jenssen, H.; Bandte, F. Über eine Neue Darstellung des Kalium-hexafluoromanganats(IV). *Angew. Chem.* **1953**, 304.
(39) Leyre, S.; Coutino-Gonzalez, E.; Joos, J. J.; Ryckaert, J.; Meuret, Y.; Poelman, D.; Smet, P. F.; Durinck, G.; Hofkens, J.; Deconinck, G.; Hanselaer, P. Absolute Determination of Photoluminescence Quantum Efficiency using an Integrating Sphere Setup. *Rev. Sci. Instrum.* **2014**, *85*, No. 123115.
(40) Hester, J. R.; Maslen, E. N.; Spadaccini, N.; Ishizawa, N.; Satow, Y. Accurate Synchrotron Radiation $\Delta\rho$ Maps for K_2SiF_6 and K_2PdCl_6. *Acta Crystallogr., Sect. B: Struct. Sci.* **1993**, *49*, 967−973.
(41) Prinsloo, L. C.; Heyns, A. M.; Ehrl, R.; Range, K. J. The Vibrational Spectra of Potassium Hexafluorosilicate, K_2SiF_6. *ChemInform* **2010**, *29*, 881−893.
(42) Deadmore, D. L.; Bradley, W. F. The Crystal Structure of K_3SiF_7. *Acta Crystallogr.* **1962**, *15*, 186−189.
(43) Stodolski, R.; Kolditz, L. Some Aspects of Real Structure and Thermal Decomposition of K_2SiF_6. *J. Fluorine Chem.* **1985**, *29*, 73.
(44) Stodolski, R.; Kolditz, L. Thermische Zersetzung von K_2SiF_6: Einfluß von Oberfläche und Wasserdampfpartialdruck. *Z. Chem.* **1985**, *25*, 190−191.
(45) Kim, Y. H.; Arunkumar, P.; Kim, B. Y.; Unithrattil, S.; Kim, E.; Moon, S.-H.; Hyun, J. Y.; Kim, K. H.; Lee, D.; Lee, J.-S.; Im, W. B. A Zero-thermal-quenching Phosphor. *Nat. Mater.* **2017**, *16*, 543−550.
(46) Shannon, R. Revised Effective Ionic Radii and Systematic Studies of Interatomic Distances in Halides and Chalcogenides. *Acta Crystallogr., Sect. A: Found. Adv.* **1976**, *32*, 751−767.
(47) Kim, M.; Park, W. B.; Bang, B.; Kim, C. H.; Sohn, K.-S. A Novel Mn^{4+}-activated Red Phosphor for Use in Light Emitting Diodes, K_3SiF_7:Mn^{4+}. *J. Am. Ceram. Soc.* **2017**, *100*, 1044−1050.
(48) Lv, L.; Jiang, X.; Huang, S.; Chen, X.; Pan, Y. The Formation Mechanism, Improved Photoluminescence and LED Applications of Red Phosphor K_2SiF_6:Mn^{4+}. *J. Mater. Chem. C* **2014**, *2*, 3879−3884.
(49) Shi, Y.; Li, W.; Wen, Y. Micro-sized K_2SiF_6:Mn^{4+} Red Phosphors for Light Emitting Diodes Synthesized by a Simple Method. *Funct. Mater. Lett.* **2017**, *10*, No. 1750016.
(50) Zhu, Y.; Huang, L.; Zou, R.; Zhang, J.; Yu, J.; Wu, M.; Wang, J.; Su, Q. Hydrothermal Synthesis, Morphology and Photoluminescent Properties of an Mn^{4+}-doped Novel Red Fluoride Phosphor Elpasolite K_2LiAlF_6. *J. Mater. Chem. C* **2016**, *4*, 5690−5695.
(51) Cady, G. H. Freezing Points and Vapor Pressures of the System Potassium Fluoride−Hydrogen Fluoride. *J. Am. Chem. Soc.* **1934**, *56*, 1431−1434.
(52) Westrum, E. F.; Pitzer, K. S. Thermodynamics of the System KHF_2-KF-HF, Including Heat Capacities and Entropies of KHF_2 and KF. The Nature of the Hydrogen Bond in KHF_2. *J. Am. Chem. Soc.* **1949**, *71*, 1940−1949.
(53) White, A. J. C.; Pistorius, C. W. F. T. Melting and Polymorphism of KHF_2, $RbHF_2$, and $CsHF_2$ to High Pressures. *J. Chem. Phys.* **1972**, *56*, 4318−4324.
(54) Opalovsky, A. A.; Fedorov, V. E.; Fedotova, T. D. Thermal Stability of Alkali Metal Bifluorides. *J. Therm. Anal.* **1970**, *2*, 373−378.
(55) Kolditz, L.; Wilde, W.; Bentrup, U. Zur Bildung der Phase K_3SiF_7 durch Thermische Zersetzung von $K_2[SiF_6]$. *Z. Chem.* **1983**, *23*, 246−247.
(56) Beurskens, G.; Jeffrey, G. A. Crystal Structure of Potassium Fluoride Tetrahydrate. *J. Chem. Phys.* **1964**, *41*, 917−923.
(57) Kasa, R.; Adachi, S. Red and Deep Red Emissions from Cubic K_2SiF_6:Mn^{4+} and Hexagonal K_2MnF_6 Synthesized in HF/$KMnO_4$/KHF_2/Si Solutions. *J. Electrochem. Soc.* **2012**, *159*, J89−J95.
(58) Arai, T.; Arai, Y.; Takahashi, T.; Adachi, S. A Yellow Phosphor K_2SiF_6 Activated by Mn^{2+} Ions. *J. Appl. Phys.* **2010**, *108*, No. 063506.
(59) Xi, L.; Pan, Y.; Huang, S.; Liu, G. Mn^{4+}Doped $(NH_4)_2TiF_6$ and $(NH_4)_2SiF_6$ Micro-crystal Phosphors: Synthesis through Ion Exchange at Room Temperature and their Photoluminescence Properties. *RSC Adv.* **2016**, *6*, 76251−76258.
(60) Yang, Z.; Wei, Q.; Rong, M.; Yang, Z.; Wang, Z.; Zhou, Q.; Wang, Q. Novel Red-emitting Phosphors A_2HfF_6:Mn^{4+} (A = Rb^+, Cs^+) for Solid-state Lighting. *Dalton Trans.* **2017**, *46*, 9451−9456.
(61) Zhou, Q.; Zhou, Y. Y.; Wang, Z. L.; Liu, Y.; Chen, G.; Peng, J. H.; Yan, J.; Wu, M. M. Fabrication and Application of Non-rare Earth Red Phosphors for Warm White-light-emitting Diodes. *RSC Adv.* **2015**, *5*, 84821−84826.
(62) Jiang, X.; Chen, Z.; Huang, S.; Wang, J.; Pan, Y. A Red Phosphor $BaTiF_6$:Mn^{4+}: Reaction Mechanism, Microstructures, Optical Properties, and Applications for White LEDs. *Dalton Trans.* **2014**, *43*, 9414−9418.
(63) Song, E.; Wang, J.; Shi, J.; Deng, T.; Ye, S.; Peng, M.; Wang, J.; Wondraczek, L.; Zhang, Q. Highly Efficient and Thermally Stable K_3AlF_6:Mn^{4+} as a Red Phosphor for Ultra-High-Performance Warm White Light-Emitting Diodes. *ACS Appl. Mater. Interfaces* **2017**, *9*, 8805−8812.
(64) Sanz-Ortiz, M. N.; Rodriguez, F. Photoluminescence Properties of Jahn-Teller Transition-metal Ions. *J. Chem. Phys.* **2009**, *131*, No. 124512.
(65) Kück, S.; Hartung, S.; Hurling, S.; Petermann, K.; Huber, G. Emission of Octahedrally Coordinated Mn^{3+} in Garnets. *Spectrochim. Acta, A* **1998**, *54*, 1741−1749.
(66) Kück, S.; Hartung, S.; Hurling, S.; Petermann, K.; Huber, G. Optical Transitions in Mn^{3+}-doped Garnets. *Phys. Rev. B* **1998**, *57*, 2203−2216.
(67) Rodriguez, F.; Aguado, F. Correlations between Structure and Optical Properties in Jahn−Teller Mn^{3+} Fluorides: A study of $TlMnF_4$ and $NaMnF_4$ under Pressure. *J. Chem. Phys.* **2003**, *118*, 10867−10875.
(68) Verstraete, R.; Sijbom, H. F.; Korthout, K.; Poelman, D.; Detavernier, C.; Smet, P. F. K_2MnF_6 as a Precursor for Saturated Red Fluoride Phosphors: the Struggle for Structural Stability. *J. Mater. Chem. C* **2017**, *5*, 10761−10769.
(69) Han, T.; Wang, J.; Lang, T.; Tu, M.; Peng, L. $K_2MnF_5{\cdot}H_2O$ as Reactant for Synthesizing Highly Efficient Red Emitting K_2TiF_6:Mn^{4+} Phosphors by a Modified Cation Exchange Approach. *Mater. Chem. Phys.* **2016**, *183*, 230−237.
(70) Deng, T. T.; Song, E. H.; Sun, J.; Wang, L. Y.; Deng, Y.; Ye, S.; Wang, J.; Zhang, Q. Y. The Design and Preparation of the Thermally Stable, Mn^{4+} Ion Activated, Narrow Band, Red Emitting Fluoride Na_3GaF_6:Mn^{4+} for Warm WLED Applications. *J. Mater. Chem. C* **2017**, *5*, 2910−2918.

DOI: 10.1021/acsami.8b01269
ACS Appl. Mater. Interfaces 2018, 10, 18845−18856

(71) Joseph, D.; Yadav, A. K.; Jha, S. N.; Bhattacharyya, D. Chemical Shift of Mn and Cr K-edges in X-ray Absorption Spectroscopy with Synchrotron Radiation. *Bull. Mater. Sci.* **2013**, *36*, 1067−1072.
(72) Zhou, K.-F.; Wang, S.-S. Spectral Properties of Weathered and Fresh Rock Surfaces in the Xiemisitai Metallogenic Belt, NW Xinjiang, China. *Open Geosci.* **2017**, *9*, 322−339.
(73) Cariati, F.; Erre, L.; Micera, G.; Piu, P.; Gessa, C. Water-Molecules and Hydroxyl-Groups in Montmorillonites as Studied by near-Infrared Spectroscopy. *Clay Clay Miner.* **1981**, *29*, 157−159.
(74) Adachi, S.; Takahashi, T. Direct Synthesis and Properties of K_2SiF_6:Mn^{4+} Phosphor by Wet Chemical Etching of Si Wafer. *J. Appl. Phys.* **2008**, *104*, No. 023512.
(75) Shao, Q.; Wang, L.; Song, L.; Dong, Y.; Liang, C.; He, J.; Jiang, J. Temperature Dependence of Photoluminescence Spectra and Dynamics of the Red-emitting K_2SiF_6:Mn^{4+} Phosphor. *J. Alloys Compd.* **2017**, *695*, 221−226.
(76) Adachi, S.; Takahashi, T. Direct Synthesis of K_2SiF_6:Mn^{4+} Red Phosphor from Crushed Quartz Schist by Wet Chemical Etching. *Electrochem. Solid-State Lett.* **2009**, *12*, J20−J23.

DOI: 10.1021/acsami.8b01269
ACS Appl. Mater. Interfaces 2018, 10, 18845−18856